Nanoscale

Synthesis of Quantum Nanocrystal-Gold Nanoshell Complex for Near Infrared Generated Fluorescence and Photothermal Decay of Luminescence

Journal:	*Nanoscale*
Manuscript ID:	NR-ART-03-2014-001721.R1
Article Type:	Paper
Date Submitted by the Author:	03-Jun-2014
Complete List of Authors:	Lin, Adam; Rice University, Bioengineering Young, Joseph; Rice University, Bioengineering Nixon, Ariel; Rice University, Bioengineering Drezek, Rebekah; Rice University, Bioengineering

Synthesis of Quantum Nanocrystal-Gold Nanoshell Complex for Near Infrared Generated Fluorescence and Photothermal Decay of Luminescence

Adam Y. Lin[ξ], Joseph K. Young[ξ], Ariel V. Nixon, Rebekah A. Drezek*
([ξ] means equal contribution)

Department of Bioengineering, Rice University, Houston, Texas

Corresponding Author Email:drezek@rice.edu

Keywords: nanocrystal, nanoshell, near-infrared, photothermal, theranostic

Abstract:

Multifunction nanoparticle complexes have previously been developed to aid physicians in both diagnosis and treatment of cancerous tissue. Here, we designed a nanoparticle complex structure that consists of a plasmonically active hollow gold nanoshell core surrounded by photoluminescent quantum nanocrystals (QNs) in the form of PbS encapsulated by a silica layer. There are three main design variables including HGN synthesis and optical tuning, formation of the silica layer on the hollow gold nanoshell surface, and fabrication and photoluminescence tuning of PbS quantum nanocrystals. The hollow gold nanoshells were deliberately designed to function in the optical regimes that maximize tissue transmissivity (800 nm) and minimize tissue absorption (1100 nm). Secondly, several chemical ligands were tested such as (3-mercaptopropyl) trimethoxysilane and mercaptoundecanoic acid for controlled growth of the silica layer. Last, PbS QNs were synthesized and optimized with various capping agents, where the nanocrystals were excited at the same wavelength used to activate the photothermal properties of the hollow gold nanoshells. Upon irradiation of the complex with a lower power 800 nm laser, the nanocrystals luminesce at 1100 nm. At ablative temperatures the intrinsic luminescent properties of the QNs is altered and the luminescent output significantly reduced (>70%). While this paper focuses on synthesis and optimization of the QN-HGN complex, in the future we believe that this novel particle complex design may have the potential to serve as a triple theranostic agent, which will aid satellite tumor localization, photothermal treatment, and ablative confirmation.

Introduction

Metallic nanoparticles (NPs) have been effective in cancer diagnostics and therapy by use of image enhancement scattering mechanisms and plasmonically generated photothermal effects for tumor ablation.[1–6] Novel multifunction NP complexes have been recently developed that combine mesoscopic properties related to morphology and surface modification for a variety of biological applications.[7–11] Hollow gold nanoshells (HGNs) are excellent photothermal agents for cancer tumor ablation.[8] Gold nanostructures possess an intense optical absorption attributed to the surface plasmon resonance phenomenon and serve as thermally stable heat transfer sources that can be utilized for photothermal therapy (PTT).[12–16] These nanoparticles are tuned to absorb light in the near infrared region (NIR), which has minimum water and hemoglobin absorption and, therefore, has the deepest optical tissue penetration depth.[17] Some of the biggest difficulties in photothermal treatment are locating of satellite tumors, identification of tumor margins, and

confirmation of complete tumor site ablation. Here, we designed a photothermally active photoluminescent nanoparticle complex that consists of a plasmonically active exciton near infrared (NIR) HGN core surrounded by photoluminescent QNs in the form of PbS..

A schematic representing the fabrication procedure of the silica encased quantum nanocrystal-hollow gold nanoshell complex (SQN-HGN) is shown in Figure 1. Briefly, HGNs is synthesized using a silver template. Then, a thin silica layer is grown on the surface of the HGN that has a silane surface modification. The NP complex design is based on a ~40 to 45 nm diameter HGN tuned to 800 nm which falls within the transparency region of the skin ~700 to 1300 nm (Supplementary Figure 1). The surface for the HGNs is modified with a 7-13 nm silica shell. This silica layer serves as both a protective shell to reinforce the structural integrity of the HGNs upon laser irradiation and as a spacer layer between the HGN and QNs. Next, the QNs are conjugated on the silica-coated HGNs, Last, the complex is encased in a final protective layer of silica.

QNs have been used as tissue imaging agents and are ideal for experiments requiring long-term photostabiltiy and high quantum yields. PbS QNs are highly tunable between 950 – 1500 nm.[18] This broad tunability makes PbS QNs advantageous in applications where deep optical tissue penetration is of concern. Optimization and synthesis is essential for this novel NP complex as there are several variables that make the fabrication process complex. Therefore, in this study, we focus on the fabrication and characterization of the NP complex. A critical challenge in design revolves around the separation between diagnosis, treatment and subsequent imaging to confirm therapeutic effect.[16] A NP complex capable of combining three phases of medical treatment, diagnosis, therapeutics and confirmation would greatly decrease time and improve efficacy of treatment. With these criteria in mind, this complex can potentially serve as a "real time" identifier of satellite tumors and allow monitoring of cancerous tissue during photothermal therapy and/or surgical removal of cancerous tissue.

To ensure tunable functions ranging from imaging to treatment to monitoring with accurate targeting of cancer specific cells, the NP complex is deliberately designed to function in the optical regimes that maximize tissue transmissivity and minimize tissue absorption (~ 800 nm and 1100 nm).[19] The QNs are also designed to excite at the same wavelength used to activate the photothermal properties of the HGNs (~808 nm). Upon irradiation of the complex with a lower power 808 nm laser the QNs are excited and fluoresces, emitting light at 1100 nm and identifying sites of interest. Once particles are identified through photoluminescence (PL) of the QNs, the optical power of the laser is increased to generate a photothermal response from the HGN cores. There is an observed temperature dependent QN luminescent response that is a direct result of the plasmonic thermal response of the HGNs. The required ablative temperature of cancerous tissue (approximately 44 to 60°C) is sufficient to significantly decrease the luminescence of the QNs. When the NPs are irradiated at sufficient laser power there will be a visible decrease in the QN emission indicating successful ablation.

Results and Discussion

HGN Synthesis and Plasmonic Properties

First, we focused on the fabrication of HGNs. HGNs, tuned to the NIR, served as the core of the nanoparticles complex. HGNs were synthesized via a galvanic reaction in which gold tetrachloroauric acid ($HAuCl_4$) was reduced onto silver nanoparticles serving as sacrificial

templates following previous procedures.[20–22] In a typical synthesis process, an aqueous solution of $AgNO_3$ and sodium citrate is heated to 60°C and then NaBH4 is added to the solution to initiate the nucleation and growth of Ag seed particles. To improve the Ag core monodispersity, the Ag seed was centrifuged at 11,000 g. This centrifuge step removed the larger seed particles producing a very monodispersed Ag seed set. If this step was not included the final nanoparticle product would resemble the polydispersed HGNs with nonuniform shells as seen in reference.[20] The monodispersed Ag seed particles were further grown by the addition of NH_2OH and additional $AgNO_3$ injection. The gold/silver galvanic reaction was then initialized by the aliquot addition of 1% $HAuCl_4$ into the solution resulting in HGNs (Figure 2A). This synthetic procedure uses the redox potential between silver and gold salt in solution. When Au^{3+} ions come in contact with the silver atoms, there is an electroless plating that reduces the Au^{3+} ions to gold atoms and oxidizes the silver to Ag^{1+} ions. For every 3 Ag atoms oxidized, a single Au atom is reduced. This 3 to 1 atom replacement leads to a gold shell hollow core structure as seen in the transmission electron microscopy (TEM) images (Figure 2B). Varying the amount of gold injection controlled the gold shell formation and subsequent growth. As the shell thickness increased the optical properties of the HGNs changed as well.

The optical properties of the HGNs were characterized using UV-vis-NIR spectroscopy. Figure 2C shows the absorbance spectra of aqueous HGNs as a function of gold addition. The optical properties of the HGN structure can be understood by examination of plasmon hybridization theory. Plasmon hybridization theory used deconstruction methods to reduce complex nanostructures into more elementary components that interact with one another to produce the hybridized plasmon modes.[23,24] The optical properties were determined by the inner and outer radius of its metallic shell layer. The core-shell dependent optical properties resulted from the plasmon response from a sphere and that of a cavity as seen in the plasmon hybridization model (Figure 2D). The cavity and sphere were electromagnetic excitations at the inner and outer interfaces of the HGN Au shell, respectively. When the sphere and cavity plasmons interact, a splitting of the plasmon resonance occurred. The two new resonances consisted of a higher energy anti-symmetric plasmon (ω+) and a lower energy symmetric plasmon (ω-) (Figure 2D). These two energies were termed the anti-bonding and bonding modes respectively. Classical Mie theory predicted that the oscillation frequencies associated with the sphere and cavity were $\omega_{sp} = \frac{\omega_B}{\sqrt{3}}$ and $\omega_{cav} = \sqrt{\frac{2}{3}}\omega_B$ respectively where ω_B is the bulk plasmon frequency.[23]

The surface charges coupled the sphere and cavity modes and the resultant hybridization depended on the difference in energies and on the Au shell thickness (Figure 2D). The hybridization modes of the HGN explained the blue shift from further Au reduction on to the initially formed Au shell (Figure 2C). The concentric shell was at its thinnest when the shell was initially formed. The thickness dictated the coupling dynamics between the sphere and cavity plasmons, which lead to plasmon splitting. For a thin shell, there was a strong coupling between the sphere and cavity, which corresponds to the lower energy-bonding mode. As the shell continued to grow and thicken, the higher energy anti-bonding mode were favored and thus reducing the coupling between the cavity and sphere, shifting the spectrum toward higher energies. Hence, the shell thickness, which was dictated by the amount of gold tetrachloroauric acid used, was critical in generating a plasmon in the near infrared region. As mentioned previously, light penetration is critical for this NP complex design. Therefore, for the final

complex, HGNs with shell thickness that were tuned to an 808 nm wavelength were selected for further synthesis and characterization.

Silica Coating of the HGNs

Since the quantum nanocrystals (QNs) need to be placed at a minimum distance to prevent fluorescence quenching by the gold surface, we focused on uniformly coating HGNs with silica shells of varying thickness. The surfaces of the HGNs could be directly coated with conformal shells of amorphous silica using the sol-gel process previously reported.[25] In this process, the formation of silica coatings involved base-catalyzed hydrolysis of tetraethyl orthosilicate (TEOS) in the presence of ammonia to generate silica sols, followed by nucleation and condensation of these sols onto the surfaces of the HGNs. Ammonia was added as a catalyst to speed up the hydrolysis of the TEOS precursor. Due to the surface charge of the HGNs, the silica preferentially reduced to the surface of the gold shell. However, silica byproducts were persistently generated during synthesis. To help facilitate the reduction of silica onto the surface of the HGN and reduce or eliminate the self-nucleation and subsequent growth of pure silica nanoparticles in solution, various functional surface ligands were studied.

HGNs were incubated with various amounts of thiol or amine terminated ligands to study the effect of silica growth using different moieties. Here, we focus on the results of HGNs functionalized MPTMS or MUA. Each surface ligand was evaluated by attempting to tune the silica shell thickness from 2 nm to greater than 30 nm in thickness. Although each ligand species formed self-assembled monolayers (SAMs) on the surface of the HGNs, the various surface moieties demonstrated different effects on the growth of the silica layer (Figure 3A-H). Great care was taken to ensure all excess thiols were removed from solution prior to the silica growth process. If an abundance of free thiols were present in solution during silica growth, there was a high probability that the thiols would have cross linked and served as silica nucleation sites leading to pure silica byproducts in solution.

Initially, HGNs functionalized with MPTMS produced a uniform shell thickness at 1 nm growth . As more silica precursors were added, thicker and rougher silica layers grew on the surface of the MPTMS functionalized HGNs. As the silica layer approached 5 nm in thickness, the surface of the NP complex became jagged and non-uniform (Figure 3B). At 15 nm thickness, large portions of the NP surface contained shoulders and long protrusions from the surface (Figure 3C). In contrast, MUA surface fictionalization produced relatively uniform silica surfaces throughout the growth process (Figure 3E-H). MUA did however lack the ability to produce uniform silica layers below 2 nm in thickness where as MPTMS formed uniform silica layers at 1 nm (Figure 3A and E). MUA was chosen as the optimum ligand to help facilitate the controlled growth of the silica shell. By using MUA and controlling experimental conditions such as the coating time and the concentration of catalyst, water, or precursor, it was possible to uniformly vary the silica shell thickness from 2 to 40 nm. Since the silica functionalized HGNs are spherical in shape and relatively monodispersed they serve as an effective foundation for the precise placement of nanocrystals within the NP complex. Silica spacer layers between 7 and 10 nm were chosen for further production of the complex. The extinction spectra of the bare HGNs and the HGNs with 7 nm silica shells were shown in Supplemental Figure 2.

Both MPTMS and MUA serve as a silane coupling agent to help facilitate the preferential reduction of silica onto the HGN surface. The reactions take place in an ethanol and ammonia rich environment where the ammonia serves as the catalysts and ethanol helps facilitate the interaction between water and TEOS. The size of the silica layer is directly related to the

nucleation and availability of TEOS. The TEOS monomer is consumed by monomers-monomer interaction to produce nuclei or addition to existing silica.

MPTMS formed a surface assembled monolayer (SAM) on the HGN surface by hydrolysis of the side chain ligands and interconnecting oxygen between the silicon atoms. The hydrolyzed orthosilicate species were closer to the HGN surface due to the reduced charge space and shorter ligand length in comparison with 11-MUA, which in turn allowed synthesis of 1 nm silica layers with MPTMS as opposed to 11-MUA. The O-Si-O groups at the surface of the MPTMS SAMs permitted faster use of monomers and increase in the polymerization rate verses the acid groups on the MUAs. The faster kinetics caused a rougher surface. As the concentration of orthosilicate increases to grow a thicker shell, an even more chaotic growth pattern occurred as the layer thickness increases. Conversely, when MUA, a longer acid terminal ligand, was used, the SAM had an extended charged space and each ligand remained independent of one another. Since the growth of silica on existing surfaces was still more preferential than self-nucleation, reduction of silica still formed onto the HGN-MUA complex instead of creating small nuclei byproducts even without the silica on the surface. The carboxyl terminal group was less vitreophilic than MPTMS and thus the silica formed at a slower rate than MPTMS, which produced a smoother layer. The HGN-MUA concentric shell at started at 2 nm thickness.

QN Synthesis and PL Tuning

Under normal conditions PbS nanocrystals are not photoluminescent above a certain size regime. In order to generate PbS nanocrystals smaller than their Bohr radius (~18 nm), capping agents are implemented. Zhao et al. demonstrated the synthesis of water soluble PbS nanocrystals stabilized with a mixture of thiols.[18] They used a combination of 1-Thioglycerol (TGL) and dithioglycerol (DTG) to produce nanocrystals possessing stable photoluminescence in the NIR spectral range of (1000-1400 nm). An alternative method to synthesize PbS nanocrystals using Zhao's work as a template was explored. Since the nanocrystals would need to be attached to the surface of the silica layer, the use of alternative thiol and amine-based capping agents possessing an end terminated silanol functional group was investigated. The use of APTES and MPTMS as a capping agent was explored individually and in combination with DTG and TGL. Briefly, PbS nanocrystals were synthesized by adding Na_2S to an oxygen expelled aqueous solution of lead (II) acetate in the presence of capping agents. By adjusting the ratio of thiols and/or amines to lead acetate used to synthesize the nanocrystals, the PbS size and emission spectrum can be tuned. Several ratios of TGL/DTG/MPTMS and TGL/DTG/APTES were used and the ratio dependent QN morphology and photoluminescent properties were studied.

The photoluminescent properties of the QNs were evaluated using a Jobin-Yvon Fluorolog-3 spectrometer equipped with a near-infrared photomultiplier tube. Two excitation sources and three irradiation wavelengths were used to independently excite the PbS QNs. Wavelength lines of 480 nm and 823 nm were isolated using a tungsten lamp as the excitation source. A 808 nm NIR laser was also used in a external optical setup to study the photoluminescent properties of the QNs. It was concluded that APTES served as a poor capping agent producing large aggregates of nanocrystals with little to no photoluminescent properties. This poor result for APTES can be attributed to the low affinity of the amine group for the PbS lattice structure in comparison to the fast processing of solution precursors during crystal growth. Thiols on the other hand readily bonded to the PbS lattice structure of sufficient size after nucleation and condensation of solution precursors. When MPTMS was used as the sole capping agent, highly polydispersed PbS nanocrystals were produced with no observable

photoluminescent properties in the 950 to 1500 nm wavelength range when excited at either 480 or 823 nm. When different concentrations of MPTMS were used in conjunction with DTG and no TGL, PbS nanocrystals presented weak photoluminescent outputs ranging from 1245 to 1255 nm wavelength. Conversely, when MPTMS was used with TGL alone, a MPTMS/TGL ratio dependent spectra was produced with a strong photoluminescent output. As the ratio of MPTMS/TGL increased from 0 to 0.5 the PL peak position shifted from 960 to 1100 nm. As the ratio continued to increase from 0.5 to 0.8 the peak position extended out to 1150 nm then blue shifted back towards 1000 nm. As the ratio approached 1 the PL intensity dramatically decreased and the peak position began to blue shift further towards 960 nm. There was also an observable change in PL intensity as a function of MPTMS/TGL ratio (Figure 4A).

When a ratio of MPTMS/TGL greater than 0.2 and less than 2 was used, PbS crystals were produced that possessed significantly higher PL intensities than the optimum ratio of DTG/TGL/Pb presented in.[18] Figure 4B showed the QN PL intensities as a function of MPTMS/TGL ratio with DTG concentration held constant. It was also observed that replacing short-ligand TGL and DTG thiols (Figure 4C and D) with longer-ligand MPTMS thiols altered the luminescent properties of the PbS nanocrystals and in some ratio cases, increased the emission intensity. A final MPTMS/TGL ratio 0.287 was selected as it produced PbS QNs with a peak position of 1100 nm and the largest PL intensity (Supplemental Figure 3).

QN-HGN Complex Formation

After the MPTMS capped QNs were synthesized, the QNs were incubated with the silica coated HGNs (Figure 5). Silanol groups exposed on the surface of the PbS nanocrystals served as anchors to covalently affix the nanocrystals to the surface of the silica functionalized HGNs. The concentration of QNs injected into the HGN solution was varied. This was in an effort to find the optimum QN concentration that would provide the most surface coverage while not generating large aggregates of the complexes. Figure 5A and C show the result of incubating a low dose and high dose concentration of QNs with silica coated HGNs. Since the QNs had exposed silanol groups it was possible for a single QN to covalently bind more than one HGN complex resulting in large HGN complex aggregates for the lower dose QNs. Several experimental conditions were implemented in order to control the binding rate of the QNs to the silica surface and prevent aggregation. It was found that a maximum of NC coverage could be achieved when the HGNs and PbS NCs were incubated in the presence of a low energy 40k Hz ultrasonic pulse (Figure 5C). The remaining exposed silanol groups on the other side of the PbS nanocrystals, not attached to the silica shell, helped facilitate the subsequent preferential reduction of silica to the surface of the nanoparticles complex, forming the final protective layer (Figure 5B and D). During the growth of the additional protective silica layer some silica byproducts were produced and observable via TEM but were successfully removed from the samples after centrifugation.

QN Temperature Effects

Since the QN-HGN complex was designed to have thermally sensitive photoluminescent properties, the effect of temperature on the optical properties of the QNs was of great importance for the proposed theranostic application. The temperature effects were studied by first exposing MPTMS/TGL capped PbS nanocrystals in aqueous solution to various temperatures. This QN study was conducted independent of the QN-HGN complex. Several solutions of capped QNs were heated in a controlled environment using a homemade laboratory heating and temperature monitoring setup. The QNs were studied over an extended temperature range (26 to 90°C). The

optical excitation was provided by a tungsten lamp with a selected line of 823 nm. The photoluminescent properties of the heated QNs in aqueous solution were evaluated using a Jobin-Yvon Fluorolog-3 spectrometer equipped with a near-infrared photomultiplier tube. Care was taken to ensure the solution cell holder did not act as a heat sink during optical measurements. Figure 6A showed the PL intensities of the NCs at various temperatures for independent samples. The inset illustrated the near linear decay PL profile as a function of temperature for temperatures 50 to 80°C which corresponds to ablation temperatures responsible for cell necrosis. The PL intensity at 26°C is taken to be the maximum PL output. As the temperature approaches 50°C the PbS NC PL intensity decreases by 70%. At 70°C the PL intensity is less than 5% output with total thermal quenching occurring at 80°C.

Further investigation of QN thermal quenching, it was noticed that several mechanisms were involved in this phenomenon.[26–29] The differences of radiative decay rates and the thermal trapping of carriers to states outside the QN core are theorized to be the main reasons for the observed PL thermal quenching at increased temperatures. These factors can be attributed to processes involved in the lowest 1S-1S exciton states. During temperature increase of the PbS QN lattice, there is a thermal escape of carriers during multi-state transitions. As the PbS lattice temperature increases, there is a thermally activated transition between the emitted states separated by an energy gap, which is a result of the exciton dark-bright-state splitting.[28] The thermally activated transition induces non-radiative relaxation into trap states. Therefore, in the quantum nanocrystals, the escape of carriers reduces the recombination rate of radiating electron-hole pairs. The PL temperature responses of the QNs make them adequately sufficient for use as temperature monitoring elements within the NP complex.

QN-HGN Photothermal Response

The PL and photothermal response of the entire silica encapsulated NP complex was evaluated by use of a continuous wave NIR 808 nm laser, micro-thermal couple, and an augmented spectrometer detection scheme with NIR photomultiplier tube. A micro-thermal couple was used to monitor the temperature of the solutions during irradiation. Care was taken in the placement of the micro-thermal couple lead to ensure avoidance of the irradiation beam cylinder. Stable suspensions of QN-HGN complexes were synthesized and placed in quartz cuvettes and stabilized to 26°C prior to irradiation. QN-HGN complexes were irradiated at different power densities while monitoring the temperature and PL output of the complex. Additionally, individual solutions of bare HGNs and bare PbS QNs were irradiated at the same irradiation powers.

To determine the thermal response of the system the QN-HGN complex solution was then irradiated at a power density of 20 W/cm^2 for 45 minutes. Figure 6B shows the measured temperature rise of a 1 mL suspension of QN-HGN complexes during irradiation. As expected, the initial heating rate was much faster than the rate after 15 minutes with the solution reaching a steady state temperature at 25 minutes. The solution temperature reached the ablative temperature zone within 2 minutes. It was also observed that the initial heating rate increased with an increase in power density (data not shown).

In a separate experiment, the PL output intensity of the QN-HGN complex was taken at room temperature at an irradiation power density low enough as to not generate a photothermal response that would increase solution temperature. A relatively low laser output power of 200 mW was chosen to prevent plasmonic photothermal activation of the HGN cores. The QN-HGN complex was irradiated with a CW 808 nm NIR laser at 0.4 W/cm^2 to determine the PL profile of

the complex prior to thermal quenching (Figure 6C). The solution temperature remained relatively unchanged when irradiate with 0.4 W/cm^2. The sample was then irradiated at a power density 20 W/cm^2 for 5 minutes. The solution temperature reached 55°C within the 5 minute irradiation window and the PL measured. The PL output intensity for the QN-HGN complex after irradiation with a power density of 20 W/cm^2 is shown in Figure 6C (dashed red line). There was a substantial decrease in PL output intensity once the complex reaches 55°C, which is in good agreement with results shown in Figure 6A for bare QNs. Figures 6B and C show that the complex can be used to identify sites of interest, generate heat, and confirm ablative temperatures were reached.

Conclusions

In summary, by combining the NIR and photothermal properties of HGNs with the luminescent properties of NIR-based QNs, we have developed a triple function theranostic NP complex that could be potentially used as a diagnostic, treatment, and therapeutic confirming agent. Using HGNs combined with QNs allow use of a single optical laser source to both excite the QNs to generate luminescence and photothermal activation of the HGNs. The QNs used in this NP complex are tuned to 1100 nm wavelength to avoid the 1000 nm absorption line of water in tissue. QNs are covalently attached to the surface of the silica layer surrounding the HGNs. The thickness of the silica spacer layer is tunable and during experimentation was varied from 2 to 30 nm. The plasmonic response of the HGNs and proximity of the QNs to the gold surface could potentially serve to enhance the luminescent properties of the QNs yet priority was given to the minimum spacer layer thickness required to prevent fluorescence quenching of the QNs by the HGNs cores. Therefore, the thickness of the silica spacer layer was finally tuned to a minimum of 7 nm in order to prevent fluorescence quenching by the HGNs. After QN conjugation another 3 to 5 nm layer of silica is grown on top encapsulating the QDs/HGN complex. The final overall NP complex size was below 90 nm in diameter. The outer silica layer is easily functionalized with biological agents for diagnosis and targeting of cancerous tissue. The plasmonic response of the HGNs enables photothermal applications and the luminescent properties of the QNs enables diagnostic and imaging capabilities. By combining the NIR and photothermal properties of HGNs with the luminescent properties of NIR-based QNs we have developed a triple function theranostic NP complex for use as a diagnostic, treatment, and therapeutic confirming agent. The QN-HGN complex consists of highly tunable optical components that enable application flexibility. This flexibility allows the complex components to be tuned to other optical regimes, both visible and NIR to fit a variety of potential applications. The defined temperature response of the QNs could be used in other applications where optical confirmation of temperature thresholds is important. Moreover, the PL quenching properties of the QNs used in this study has universality and could be extended or replaced by other chalcogenide-based fluorescent structures such as Ag_2S.This complex design and functionality could greatly aid in the identification of tumor margins and satellite tumors while allowing for ablative confirmation.

Experimental

Reagents: Hydrogen tetrachloroaurate III trihydrate (HAuCl4·3H2O, 99.99%), silver nitrate (AgNO3, 99%), tetraethyl orthosilicate (Si(OC2H5)4, 999.99%), hydroxylamine hydrochloride (NH2O HCl, 94%), sodium citrate (99%), sodium borohydride (NaBH4, 99%),

lead (II) acetate trihydrate (99.99%), 1-Thioglycerol (TGL, 95%), dithioglycerol (DTG, 95%), 3-mercaptopropyl trimethoxysilane (MPTMS, 95%), sodium sulfide nonahydrate (Na2S, 99.99), triethylamine ((C2H5)3N, 99%), ammonia hydroxide (NH3, 28-30%), ethanol 200 proof absolute, 3-Aminopropyl triethoxysaline (APTES, 98%), 11-Mercaptoundecanoic acid (MUA, 98%), and absolute ethanol (C2H5OH, 99.5%) where purchased from Sigma Aldrich and used as received. Argon gas (Ar, 99.98%) and nitrogen gas (N, 99.99%) was supplied by Matheson-Trigas. All solutions were prepared using ultrapure water (18 Mohm Millipore Milli-Q water).

Pre-synthesis: All glassware used in the following procedures were cleaned in a bath of freshly prepared aqua regia solution (3 parts HCL acid to 1 part HNO3 acid) and rinsed thoroughly with ethanol three times and then rigorously rinsed four times with copious amounts of pure grade water and oven dried prior to use. Stirring was conducted by a PTFE-coated magnetic stir bar which was cleaned and dried in the same manner as the glassware. Plastic beakers and micro centrifuge tubes were washed using detergent then vigorously rinsed using ethanol and Milli-Q water.

Synthesis of HGNs: HGNs were synthesized using galvanic replacement of silver with gold. We carried out the synthesis by creating Ag cores to serve as sacrificial templates. First, aqueous solutions of AgNO3 0.2 mM was combined with sodium citrate 0.5 mM and allowed to age at least 12 hours in amber bottles. Additional solutions of AgNO3 0.1 M and HAuCl4 25 mM were allowed to age and set aside for further use. 50 mL of 0.2 mM silver nitrate/sodium citrate solution was heated using a stir plate to 60°C. 1 mL of 100 mM of NaBH4 was injected into the solution under rapid stirring. The solution was allowed stir for 2 hours. After cooling the particles were centrifuged at 11,000 g for a minimum of 20 minutes. The larger Ag seed particles were discarded and the smaller monodispersed seed particles resuspended in solution. 1 mL of 200 mM hydroxylamine was added to the Ag seed and stirred for 5 minutes. Then 50 to 200 uL of 0.1 M AgNO3 solution was injected to grow the Ag cores. The cores were aged overnight. The Ag cores temperature was raised to 60°C and injected with various amounts of 25 mM HAuCl4 drop wise. To tune the HGNs to 800 nm wavelength small volumes of Ag cores were placed in cuvettes and small additions of Au added. Once the HGNs were tuned then the synthesis process was scaled.

Synthesis of QNs: The synthesis of PbS QNs were conducted in the presence of varying capping agents in the form of MPTMS, DTG, TGL, and APTES similar to procedures of reference [2]. First, 15 mL of an aqueous solution containing 0.25 mM of lead (II) acetate and various amounts of MPTMS or APTES was adjusted to pH = 11.2 by adding triethylamine. Then 0.1 M solution of sodium sulfide was injected while the solution was under rapid stirring. When APTES or MPTMS was used as the sole stabilizer the resultant QNs were polydispersed. When TGL and/or DTG were used in addition to MPTMS and APTES QNs tunable PL were produced.

When TGL was used with APTES or MPTMS alone, 1.5 mM of TGL was added to the 15 mL lead (II) acetate solution and the concentration of MPTMS or APTES was varied from 0 to 0.6 mM. When DTG was used with APTES or MPTMS alone, 0.96 mM of DTG was added to the 15 mL led (II) acetate solution and the concentration of MPTMS or APTES was varied from 0 to 0.6 mM. When both TGL and DTG were used, 1.5 mM of TGL and 0.96 mM of DTG were injected into the 15 mL lead (II) acetate solution and the concentration of MPTMS or APTES

was varied from 0 to 0.6 mM. All QNs were produced at room temperature and aged overnight in the dark prior to PL measurements or conjugation to the silica coated HGNs.

QN-HGN Complex Formation: Prior to silica growth, HGNs were either functionalized with MPTMS or MUA. HGNs were functionalized with MPTMS or MUA by first washing the HGNs in water at 2200 g for 20 minutes. The HGNs were resuspended in 36 mL water and 1 mL of 1% tween solution was added and allowed to stir for 5 minutes. Next 4 mL of ethanol was added to the solution. 10 uL of MPTMS from the stock bottle was added to 1 mL of ethanol. Then 100 uL of that solution was added to the HGNs. The solution was allowed to stir overnight. For MUA functionalization, a 1 M stock solution was made in ethanol and the same procedure used for MPTMS was followed.

After surface functionalization, HGNs were washed and resuspended in ethanol. HGNs were coated with silica by first diluting 500 uL of TEOS in 500 uL of ethanol for a 50% vol solution. Next, 100 uL of NH4OH was diluted in 0.9 mL of ethanol for a final NH4OH concentration 2.8% in 1000 uL. 790 uL of HGN solution was were placed in plastic tubes. 50 uL of the diluted NH4OH solution and 160 uL of water was added and vortexed. Next, varying amounts of diluted TEOS was added to the tubes while under ultrasonic pulsation. The solution was allowed to react for 45 minutes. Afterwards the solution was centrifuged at 7000 rcf for 20 minutes. The silica coated HGNs were washed twice more in ethanol and resuspended in ethanol.

The MPTMS functionalized QNs were incubated with the silica coated HGNs at various QNs concentrations in the presence of a low power ultrasonic pulse. Excess QNs were removed via centrifugation and the HGN resuspended in ethanol. After successful conjugation of the QNs to the surface a final silica layer was grown over the QNs. To grow the final 2 to 5 nm layer QN-HGN solutions were adjusted to 790 uL in volume. 20 to 50 uL of diluted NH4OH and 160 uL of water was added and vortexed. Varying amounts of diluted TEOS solution was added in the presence of an ultrasonic pulse and allowed to react for 45 minutes. After 45 minutes the particles were centrifuged at 7000 rcf for 20 minutes and washed twice more in ethanol. The particles were resuspended in either water or ethanol.

Nanoparticle Characterization: Nanoparticle size distributions, surface characterizations, and morthphologies were determined by transmission electron microscopy (TEM) performed using a JEOL 2010 and JEOL 2100 Field Emission Gun Transmission Electron Microscope operating at 120 kV and 200 kV respectively. Samples were prepared by contacting a nanoparticle (10μL) drop with a carbon film coated 200 mesh copper grid. The grids were placed in a spotlessly clean container, covered and allowed to dry completely before use.

The optical response of the HGNs was determined by examining the optical extinction spectra of aqueous samples in 1 cm path length quartz cuvettes using a Varian Cary 300 UV-visible spectrophotometer. The UV-visible spectra were acquired at wavelengths between 400 to 900 nm. Distilled water was used as The photoluminescent properties of the QNs were evaluated using a Jobin-Yvon Fluorolog-3 spectrometer equipped with a near-infrared photomultiplier tube. Two excitation sources and three irradiation wavelengths were used to independently excite the PbS NCs. Wavelength lines of 480 nm and 823 nm were isolated using a tungsten lamp as the excitation source. A 808 nm NIR laser was also used in a homemade laboratory optical setup to study the photoluminescent properties of the QNs.

The temperature response of the standalone QNs was conducted by heating the QNs on a hot plate and monitoring the temperature using a thermocouple. Once a specific temperature was reached the PL output was measured. The temperature response of the PL for the entire complex

was examined by first irradiating the complex at 200 mW with a CW NIR laser while simultaneously measuring the PL intensity. Afterwards, the laser power density was increased to 20 W/cm^2 and irradiated for 5 minutes. Once the temperature of the solution reached 55°C the PL output intensity was again measured. The photothermal temperature response of the system was measured by irradiating 1.5 mL of NP solution at a power density of 20 W/cm^2 for 45 minutes and measuring the temperature with a thermocouple.

Supporting Information

Supporting information is available online. Supporting information contains supplemental figures 1, 2 and 3.

Acknowledgment.

The authors acknowledge Allen Chen and Aaron Foster for research input, helpful discussions related to material properties and applications, and for proofreading. These studies were supported by the Welch Foundation (Grant No. C-1598). A. Lin received support from the Medical Scientist Training Program at Baylor College of Medicine, the Edward and Josephine Hudson Scholarship, and the Ruth L. Kirschstein National Research Service Awards for Individual Predoctoral MD/PhD Fellows (F30) by NIH and NCI.

References

1. J. C. Ostrowski, A. Mikhailovsky, D. A. Bussian, M. A. Summers, S. K. Buratto, and G. C. Bazan, *Adv. Funct. Mater.*, 2006, **16**, 1221–1227.

2. J. N. Anker, W. P. Hall, O. Lyandres, N. C. Shah, J. Zhao, and R. P. Van Duyne, *Nat. Mater.*, 2008, **7**, 442–53.

3. C. J. Murphy, A. M. Gole, J. W. Stone, P. N. Sisco, A. M. Alkilany, E. C. Goldsmith, and S. C. Baxter, *Acc. Chem. Res.*, 2008, **41**, 1721–30.

4. M. L. Juan, M. Righini, and R. Quidant, *Nat. Photonics*, 2011, **5**, 349–356.

5. L. R. Bickford, J. Chang, K. Fu, J. Sun, Y. Hu, A. Gobin, T.-K. Yu, and R. A. Drezek, *NanoBiotechnology*, 2008, **4**, 1–8.

6. L. R. Bickford, R. J. Langsner, J. Chang, L. C. Kennedy, G. D. Agollah, and R. Drezek, *J. Oncol.*, 2012, **2012**, 291898.

7. W. Lu, C. Xiong, G. Zhang, Q. Huang, R. Zhang, J. Z. Zhang, and C. Li, *Clin. Cancer Res.*, 2009, **15**, 876–86.

8. M. P. Melancon, W. Lu, Z. Yang, R. Zhang, Z. Cheng, A. M. Elliot, J. Stafford, T. Olson, J. Z. Zhang, and C. Li, *Mol. Cancer Ther.*, 2008, **7**, 1730–9.

9. L. C. Kennedy, A. S. Bear, J. K. Young, N. A. Lewinski, J. Kim, A. E. Foster, and R. A. Drezek, *Nanoscale Res. Lett.*, 2011, **6**, 283.

10. X. Huang, W. Qian, I. H. El-Sayed, and M. A. El-Sayed, *Lasers Surg. Med.*, 2007, **39**, 747–53.

11. J. K. Young, N. A. Lewinski, R. J. Langsner, L. C. Kennedy, A. Satyanarayan, V. Nammalvar, A. Y. Lin, and R. A. Drezek, *Nanoscale Res. Lett.*, 2011, **6**, 428.

12. L. B. Carpin, L. R. Bickford, G. Agollah, T.-K. Yu, R. Schiff, Y. Li, and R. a Drezek, *Breast Cancer Res. Treat.*, 2011, **125**, 27–34.

13. E. S. Day, L. Zhang, P. A. Thompson, J. A. Zawaski, C. C. Kaffes, M. W. Gaber, S. M. Blaney, and J. L. West, *Nanomedicine (Lond).*, 2012, **7**, 1133–48.

14. C. Loo, A. Lowery, N. Halas, J. West, and R. Drezek, *Nano Lett.*, 2005, **5**, 709–11.

15. L. C. Kennedy, L. R. Bickford, N. a Lewinski, A. J. Coughlin, Y. Hu, E. S. Day, J. L. West, and R. a Drezek, *Small*, 2011, **7**, 169–83.

16. J. K. Young, E. R. Figueroa, and R. a Drezek, *Ann. Biomed. Eng.*, 2012, **40**, 438–59.

17. R. Weissleder, *Nat. Biotechnol.*, 2001, **19**, 316–7.

18. X. Zhao, I. Gorelikov, S. Musikhin, S. Cauchi, V. Sukhovatkin, E. H. Sargent, and E. Kumacheva, *Langmuir*, 2005, **21**, 1086–90.

19. S. L. Jacques, *Phys. Med. Biol.*, 2013, **58**, R37–61.

20. B. G. Prevo, S. a Esakoff, A. Mikhailovsky, and J. a Zasadzinski, *Small*, 2008, **4**, 1183–95.

21. V. Vongsavat, B. M. Vittur, W. W. Bryan, J.-H. Kim, and T. R. Lee, *ACS Appl. Mater. Interfaces*, 2011, **3**, 3616–24.

22. Y. Sun, B. Mayers, and Y. Xia, *Adv. Mater.*, 2003, **15**, 641–646.

23. E. Prodan, P. Nordlander, and N. J. Halas, *Nano Lett.*, 2003, **3**, 1411–1415.

24. H. Wang, D. W. Brandl, P. Nordlander, and N. J. Halas, *Acc. Chem. Res.*, 2007, **40**, 53–62.

25. Y. Lu, Y. Yin, Z.-Y. Li, and Y. Xia, *Nano Lett.*, 2002, **2**, 785–788.

26. L. Turyanska, A. Patanè, M. Henini, B. Hennequin, and N. R. Thomas, *Appl. Phys. Lett.*, 2007, **90**, 101913.

27. M. S. Gaponenko, N. a. Tolstik, A. a. Lutich, A. a. Onushchenko, and K. V. Yumashev, *Phys. E Low-dimensional Syst. Nanostructures*, 2013, **53**, 63–65.

28. M. S. Gaponenko, A. A. Lutich, N. A. Tolstik, A. A. Onushchenko, A. M. Malyarevich, E. P. Petrov, and K. V Yumashev, 2010, 1–9.

29. N. Pendyala and K. K. Rao, *J. Lumin.*, 2008, **128**, 1826–1830.

Figures

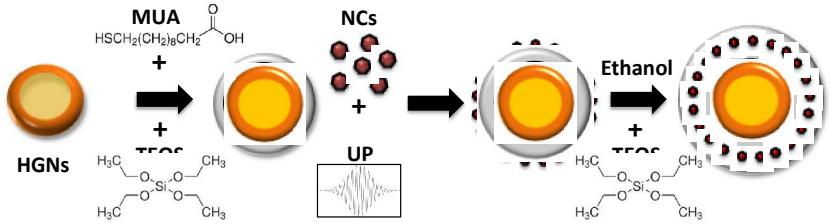

Figure 1. Schematic representing the fabrication steps for the silica encased quantum nanocrystals-hollow gold nanoshell complex.

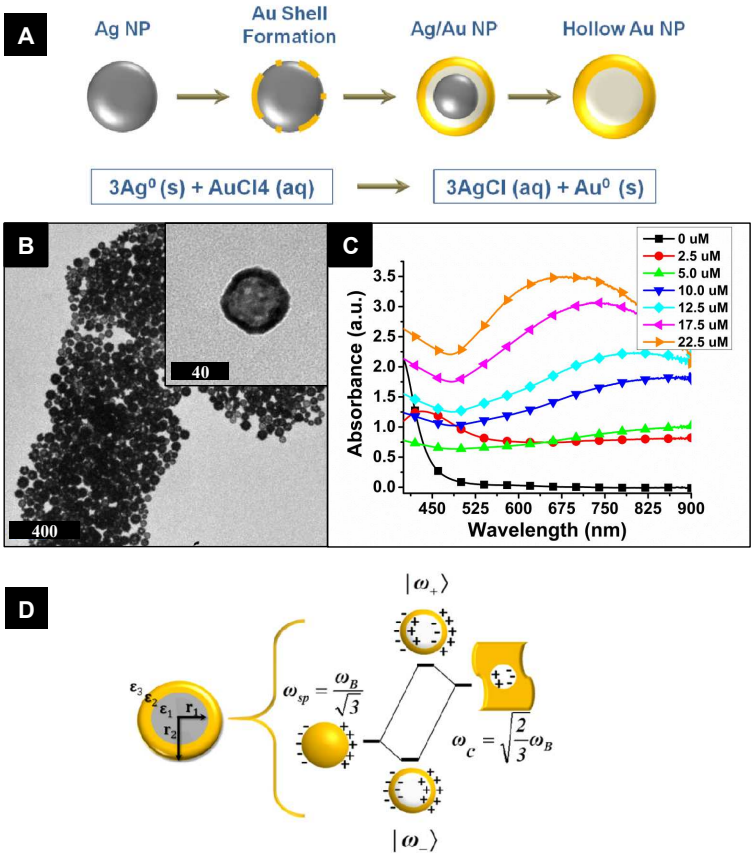

Figure 2. (A) Schematic representing the galvanic replacement of the silver core with gold. As gold reduces to the surface of the of the silver core, silver atoms are exchanged with gold atoms that eventually leads to complete etching of the silver core. (B) TEM image of HGNs synthesized via galvanic replacement exchange of silver and gold atoms. (C) UV-Vis-NIR extinction spectra of HGNs with varying amounts of gold salt addition. (D) Geometric description of HGN and energy level diagram depicting plasmon hybridization in HGNs. The plasmon hybridization is a result of sphere cavity coupling that splits the plasmon into an anti-symmetric "anti-bonding" and symmetric "bonding" mode.

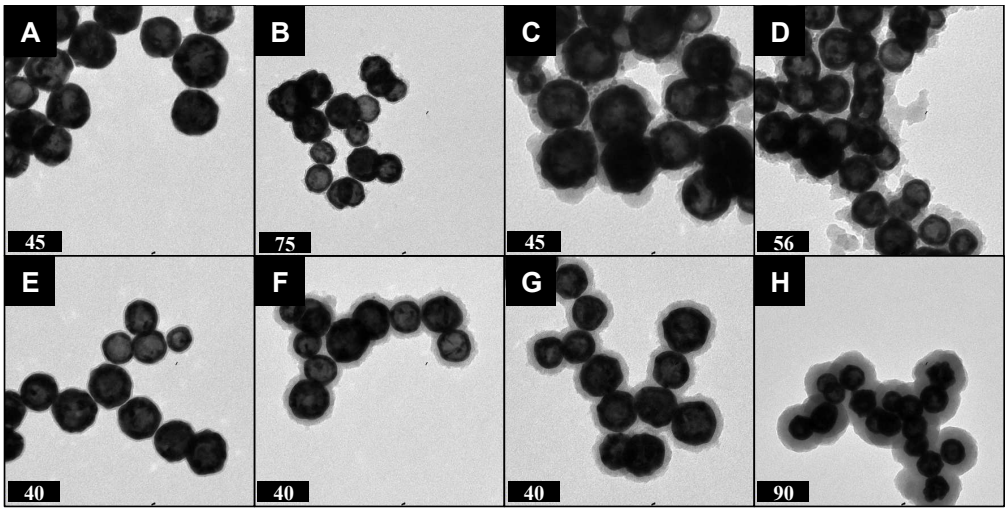

Figure 3. TEM images of silica coated HGNs. A-D represent HGNs functionalized with MPTMS and silica grown to various shell thicknesses: (A) 1 nm, (B) 5 nm, (C) 15 nm, and (D) up to 20 nm but highly non-uniform. E-H represent HGNs functionalized with MUA and silica grown to various shell thicknesses: (E) 2 nm, (F) 10 nm, (G) 15 nm, and (H) 30 nm.

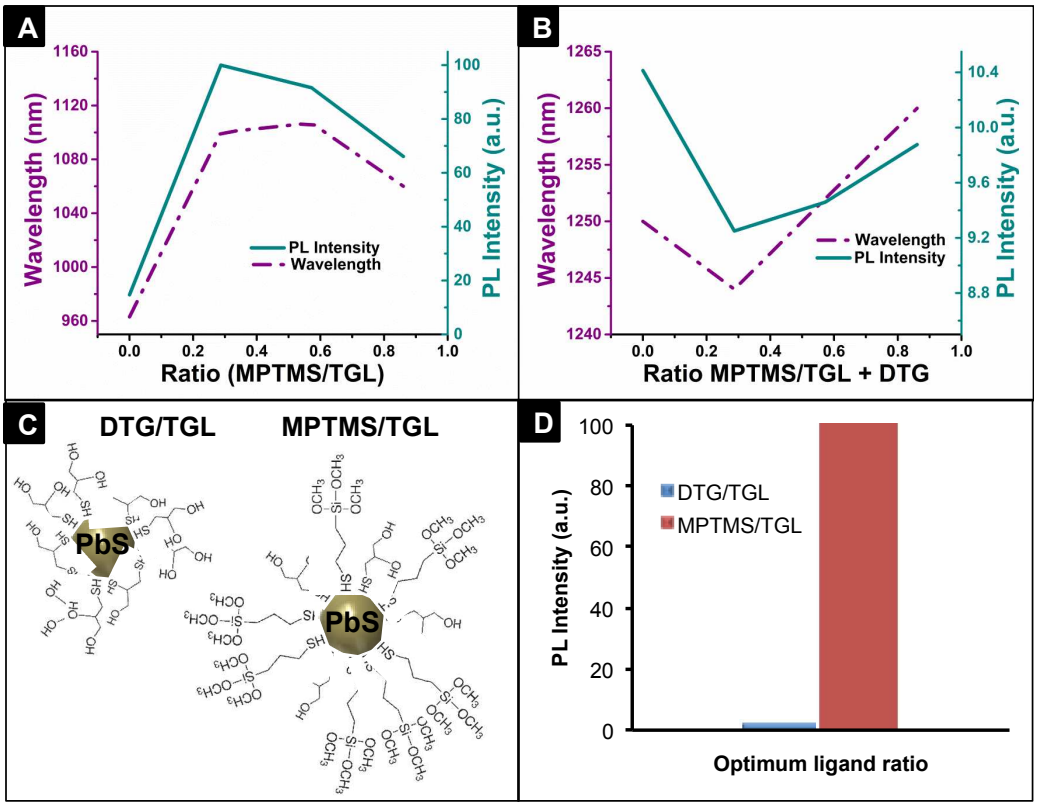

Figure 4. (A) Quantum nanocrystal PL intensity and wavelength peak position as a function of MPTMS/TGL ratio. (B) Quantum nanocrystal PL intensity and wavelength peak position as a function of MPTMS/TGL ratio with DTG concentration held constant. A MPTMS/TGL ratio of 0.0 corresponds to the optimum ratio of TGL and DTG according to literature. (C) Diagram of PbS QNs functionalized with DTG/TGL alone (left) and MPTMS/TGL alone (right). This figure

serves as a quality illustration of the surface dynamics of a shorter ligand (DTG) vs. a longer ligand (MPTMS) thiol molecule. (D) Bar graph shows the PL intensity difference when using MPTMS in place of DTG. The DTG/TGL ratio is the optimum ratio used to synthesize PbS QNs taken from literature.

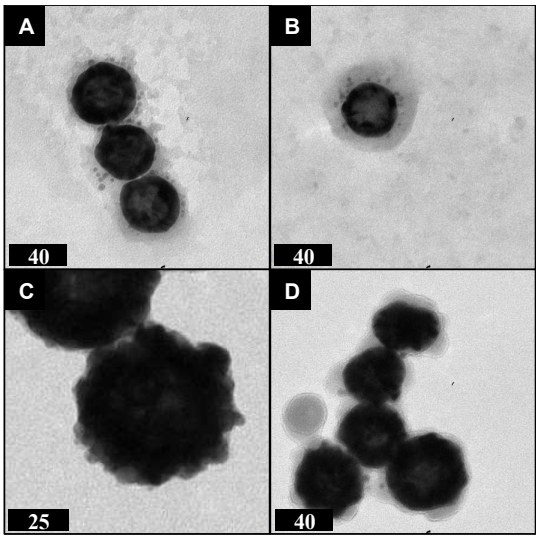

Figure 5. TEM images of quantum nanocrystal attachment to silica coated HGNs. (A) TEM image of QN functionalized silica coated HGNs using a lose dose concentration of QNs. (B) Final silica coating of QN-HGN complex after incubation with low dose concentration of QNs. (C) TEM image of functionalized silica coated HGNs using a high dose concentration of QNs. (D) Final silica coating of QN-HGN complex after incubation with high dose concentration of QNs.

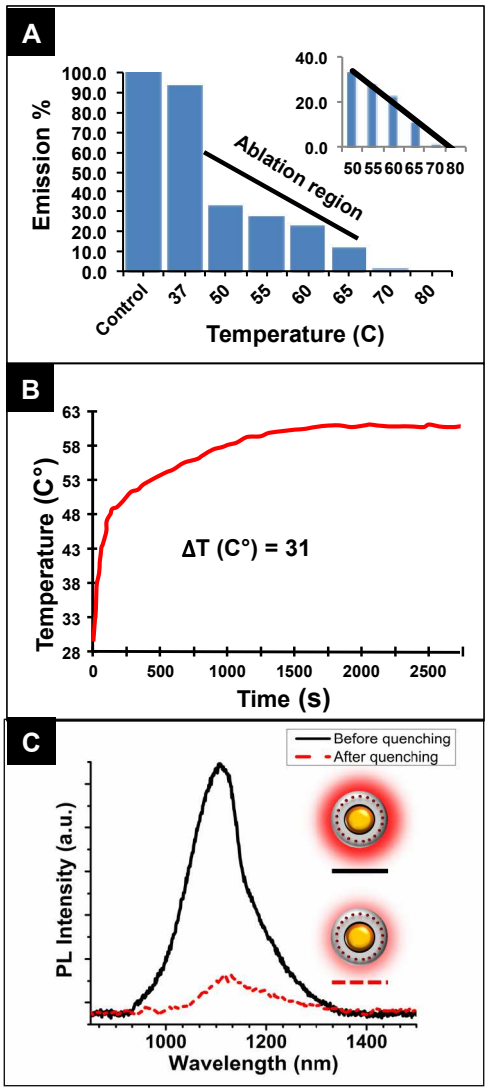

Figure 6. (A) Bar graph describing the temperature dependent PL output of MPTMS capped quantum nanocrystals. The "Control" represents 100% maximum PL intensity taken at 26°C. The inset shows the near linear PL intensity decay associated with temperatures that fall within the ablation temperature region. (B) Experimental calorimetric data showing the degree of heating of a 1mL volume of QN-HGN solution at a power density of 20 W/cm2 for 45 minutes. (C) PL spectra of the QN-HGN complex before (solid black line) and after (red dotted line) thermal quenching. Sample was irradiated at a power density of .4 W/cm2. The power density was raised to 20 W/cm2 to induce thermal quenching of the NP complex. The inserted QN-HGN complex models serve as a qualitative illustration of the PL quenching as a result of ablative power density increase.